Geophysical Journal International

Geophys. J. Int. (2021) **224,** 1371–1380
Advance Access publication 2020 November 05
GJI Seismology

doi: 10.1093/gji/ggaa524

Stress drop–magnitude dependence of acoustic emissions during laboratory stick-slip

Aglaja Blanke [1], Grzegorz Kwiatek,[1,2] Thomas H. W. Goebel,[3] Marco Bohnhoff[1,2] and Georg Dresen[1,4]

[1] *GFZ German Research Centre for Geosciences, Geomechanics and Scientific Drilling, Telegrafenberg, D-*14473 *Potsdam, Germany. E-mail: a_blanke@gfz-potsdam.de*
[2] *Department of Earth Sciences, Free University Berlin, Malteserstraße* 74–100*, D-*12249 *Berlin, Germany*
[3] *Center for Earthquake Research and Information, University of Memphis,* 3890 *Central Avenue, Memphis, TN* 38152*, USA*
[4] *Institute of Geosciences, University of Potsdam, Karl-Liebknecht-Str.* 24–25*, D-*14476 *Potsdam-Golm, Germany*

Accepted 2020 November 2. Received 2020 October 27; in original form 2020 May 19

SUMMARY

Earthquake source parameters such as seismic stress drop and corner frequency are observed to vary widely, leading to persistent discussion on potential scaling of stress drop and event size. Physical mechanisms that govern stress drop variations are difficult to evaluate in nature and are more readily studied in controlled laboratory experiments. We perform two stick-slip experiments on fractured (rough) and cut (smooth) Westerly granite samples to explore fault roughness effects on acoustic emission (AE) source parameters. We separate large stick-slip events that generally saturate the seismic recording system from populations of smaller AE events which are sensitive to fault stresses prior to slip. AE event populations show many similarities to natural seismicity and may be interpreted as laboratory equivalent of natural microseismic events. We then compare the temporal evolution of mechanical data such as measured stress release during slip to temporal changes in stress drops derived from AEs using the spectral ratio technique. We report on two primary observations: (1) In contrast to most case studies for natural earthquakes, we observe a strong increase in seismic stress drop with AE size. (2) The scaling of stress drop with magnitude is governed by fault roughness, whereby the rough fault shows a more rapid increase of the stress drop–magnitude relation with progressing large stick-slip events than the smooth fault. The overall range of AE sizes on the rough surface is influenced by both the average grain size and the width of the fault core. The magnitudes of the smallest AE events on smooth faults may also be governed by grain size. However, AEs significantly grow beyond peak roughness and the width of the fault core. Our laboratory tests highlight that source parameters vary substantially in the presence of fault zone heterogeneity (i.e. roughness and narrow grain size distribution), which may affect seismic energy partitioning and static stress drops of small and large AE events.

Key words: Acoustic properties; Body waves; Earthquake dynamics; Earthquake source observations; Dynamics and mechanics of faulting.

1 INTRODUCTION

Since the late 1960s, there is a debate on whether earthquake source parameters, and thus rupture processes, are self-similar across magnitude scales or show a scale dependence. A plethora of studies exists that analysed stress drop across a range of earthquake magnitudes (e.g. Aki 1967; Ide & Beroza 2001, Ide *et al.* 2003; Allmann & Shearer 2009; Baltay *et al.* 2011; Abercrombie 2013; Cocco *et al.* 2016). The static stress drop is the difference between initial and final shear stress spatially averaged over the rupture surface (e.g. Aki 1967; Brune 1970; Candela *et al.* 2011; Cotton *et al.* 2013). A constant stress drop indicates a self-similar source process irrespective of the event magnitude.

The static stress drop is an important source parameter that relates to the energy budget of seismic events (e.g. Kanamori & Rivera 2006) and also affects near-field ground motions (e.g.

Spottiswoode 1993). Hence, it is an important parameter in seismic hazard and risk assessment and it is commonly used to establish ground motion prediction equations (e.g. Cotton *et al.* 2013; Huang *et al.* 2017, Baltay *et al.* 2019).

It is difficult to estimate stress drop accurately from seismic data mainly due to uncertainties in the assessment of corner frequency, model-dependence and error propagations. Many studies discuss potential stress drop dependence on seismic moment or rupture dimension (e.g. Aki 1967; Abercrombie 1995; Ide *et al.* 2003, Kwiatek *et al.* 2011; Cocco *et al.* 2016). Indeed, stress drop estimates averaged across the entire bandwidth of earthquake magnitudes ($-9 < M < 8$) suggest a global average value of a few MPa (e.g. Cocco *et al.* 2016). However, the individual data sets display varying average stress drops spanning over some decades (e.g. Kanamori & Brodsky 2004; Allmann & Shearer 2009; Kwiatek *et al.* 2011; Cotton *et al.* 2013; Cocco *et al.* 2016; Huang *et al.* 2016). In some cases, observed deviations from constant stress drop may be related to non-physical factors including site-, path- and/or sensor-related effects, limited recording bandwidth, insufficient station coverage, inadequate sensor-rock coupling, incorrect or specific source model assumptions, and error propagation in parameter estimates (e.g. Ide & Beroza 2001; Ide *et al.* 2003). In general, stress drop estimates can be improved by using high-quality seismic data recorded over a wide frequency band and appropriate waveform processing techniques (e.g. Shearer *et al.* 2019). However, studies clearly indicate a scatter of estimated stress drops ranging from 0.01 to 100 MPa, thus significantly exceeding internal uncertainties originating from non-physical factors. This suggests stress drop varies possibly also due to different physical processes in the earthquake source (e.g. Cocco *et al.* 2016). Fault properties (e.g. composition, roughness and geometry) and heterogeneous stress conditions may cause stress drops to vary (e.g. Sagy *et al.* 2007; Candela *et al.* 2011; Cocco *et al.* 2016; Baltay *et al.* 2019).

Current data quality of natural and induced seismic waveforms likely limits the resolution of the derived physical parameters governing source mechanics. Since the pioneering work of Brace & Byerlee (1966), laboratory experiments are known to contribute to a better understanding of the physics of natural earthquakes (Beeler 2006). That is, because the boundary conditions in the laboratory can be controlled and experiments can be repeated. Recent studies, analysing source and statistical properties of natural and laboratory seismic activity (e.g. McGarr & Fletcher 2003; Thompson *et al.* 2009; Goebel *et al.* 2013; Yoshimitsu *et al.* 2014), indicate similarity of physical earthquake processes across a broad range of scales. Thus, seismic rupture processes down to the submillimetre scale can be studied by analysing high-frequency acoustic emission events (AEs, e.g. Bohnhoff *et al.* 2009).

Only few laboratory studies exist that analyse stress drops of AEs in detail (e.g. G31; McLaskey *et al.* 2014; Yoshimitsu *et al.* 2014). An exact sensor calibration to determine absolute event magnitudes for AEs is complicated, because sensor response is affected by confining pressure, sensor coupling and orientation (e.g. Plenkers *et al.* 2011). Consequently, a comparison of absolute AE stress drops in the laboratory with stress drops of natural tectonic earthquakes can be difficult. Nevertheless, stress drop differences between experiments with similar sensors can be compared with much higher confidence. Such a comparison is the main focus of the present study.

We analysed AE events of two laboratory stick-slip experiments on Westerly granite samples to resolve the impact of fault surface roughness and fault core width (*cf.* Goebel *et al.* 2014b) on seismic source characteristics. In general, Westerly granite is chosen for laboratory experiments because it represents abundant crystalline rocks of the continental upper crust. Its isotropic texture (e.g. Goebel *et al.* 2012) facilitates the analysis of seismic AE data. The recorded AEs cover a large moment magnitude range ($-9 < M_W < -5.6$) compared to previous AE studies mentioned above. Both seismic and mechanical data were measured throughout the experiments. The mechanical data provide a direct estimate of the differential stress released during stick-slip, that is, the mechanical stress drop ($\Delta\sigma_m$) (we distinguish mechanical ($\Delta\sigma_m$) and seismic ($\Delta\sigma_{AE}$) stress drop, based on how the measurement was made, that is, force cell for $\Delta\sigma_m$ vs AE sensors for $\Delta\sigma_{AE}$. The seismic waveform recordings were clipped during the large slip events, preventing detailed source parameter studies of the associated largest AEs. However, unclipped waveforms were recorded for smaller AE events during the interslip periods. These are thought to represent the analogue of earthquakes during the interseismic period between two large tectonic earthquakes. We used these waveforms to determine corner frequencies and seismic moments of AE populations prior to larger slip events within the rock specimen by applying the spectral ratio method (e.g. Ide *et al.* 2003; Abercrombie & Rice 2005; Kwiatek *et al.* 2011; Harrington *et al.* 2015). Changes in source characteristics of these AE populations are thought to image changes in fault stress state as detailed below. It should be noted that the seismic stress drop ($\Delta\sigma_{AE}$) estimates for AE events are not directly connected to mechanical stress drop $\Delta\sigma_m$. Furthermore, $\Delta\sigma_{AE}$ is primarily a measure of the proportion of high-frequency energy radiation for events of a given magnitude that reflects stress release on the microscale using several assumptions about rupture velocity and aspect ratio (e.g. Aki 1967; Brune 1970).

2 EXPERIMENTAL SETUP AND DATA

AE waveform data was recorded during laboratory triaxial stick-slip experiments performed at room temperature on two cylindrical oven-dried Westerly granite samples (*cf.* Goebel *et al.* 2012; Kwiatek *et al.* 2014a). Westerly granite exhibits grain sizes between 0.05 and 2.2 mm with an average grain size of 0.75 mm (e.g. Tullis & Yund 1977; Goebel *et al.* 2014a). The experiments were performed in a servo-controlled loading frame (MTS-815, Material Testing Systems) equipped with a pressure vessel and samples were placed in a rubber jacket to prevent intrusion of hydraulic confining oil. To monitor AE activity, 16 piezoceramic transducers with a resonance frequency of about 2 MHz were placed in brass casings, which were attached directly to the sample surface and in top and bottom pistons, respectively. Full waveform data were recorded using a transient recording system (DAX-Box, Prökel, Germany) in triggered mode at a sampling frequency of 10 MHz and an amplitude resolution of 16 bits. In addition, horizontal and vertical *P*-wave velocities were measured at regular 30 s intervals during the experiments, using active ultrasonic pulse transmissions. Time-dependent velocity measurements were used to locate AE events and assess the evolution of damage in the sample.

We report on two different experiments (*cf.* Fig. 1): (1) experiment S12 was done on a saw-cut sample of 105 mm height and 50 mm diameter, cut at 30° to the vertical axis across. The saw-cut surface was roughened with a coarse silicon carbide powder (60 grit). Prior to loading, sample S12 was subjected to a constant confining pressure (P_c) of 133 MPa and then loaded in axial compression (σ_1) using a strain rate of 3×10^{-4} mm s^{-1}.

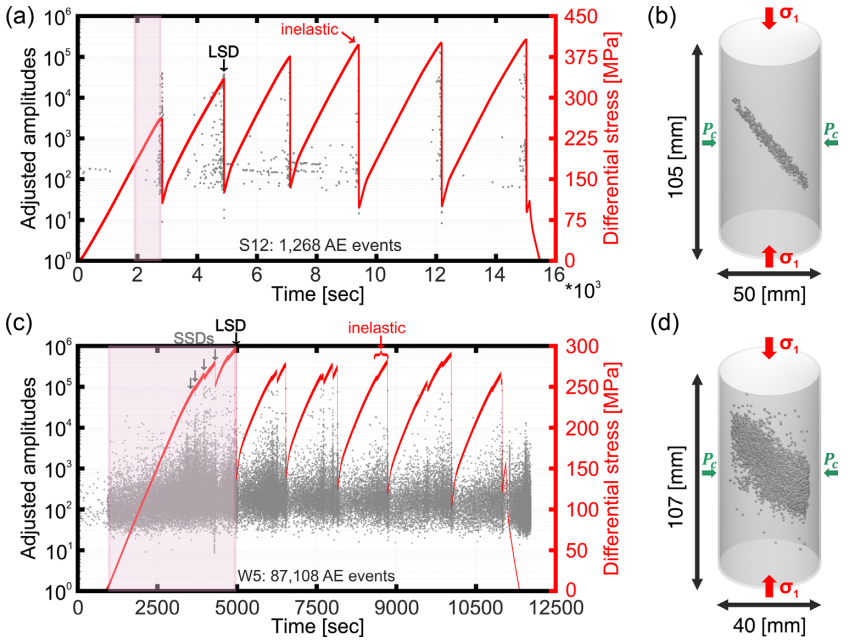

Figure 1. Differential stress (red curve) and AE amplitude (grey dots) as a function of time from start of experiments (a) S12 and (c) W5. Examples of inelastic deformation phases are marked and labelled in red. Grey arrows indicate examples of SSDs (small mechanical stress drops) and black arrows indicate examples of LSDs (large mechanical stress drops). Shaded rectangles exemplify event populations used for demonstrating the regression analysis in Figs 2(a) and (b). (b) and (d) Spatial distribution of AEs (dots) within samples S12 and W5, respectively. Locations of AEs reflect a simple fault zone for S12 and a complex fault zone for W5. Bold arrows indicate axial stress (σ_1) and confining pressure (P_c).

(2) Experiment W5 was conducted on a cylinder (107 mm x 40 mm) with Teflon-filled saw-cut notches of 1.9 cm length at 30° inclination to the vertical axis. Sample W5 was then fractured at 75 MPa resulting in a complex rough fault. The fault was locked by increasing P_c to 150 MPa and subsequently activated in a series of stick-slip events at an axial strain rate of 3×10^{-6} mm s^{-1}.

3 METHOD

3.1 Data pre-processing

P-wave onsets of AEs and first *P*-wave amplitudes were automatically picked using the Akaike information criterion (e.g. Stanchits *et al.* 2006). AE hypocentres were estimated using a hybrid grid search-simplex algorithm assuming a time-dependent anisotropic velocity model derived from ultrasonic transmission data (G43). The estimated location accuracy of AE hypocentres is about ± 2 mm (e.g. Stanchits *et al.* 2006; Goebel *et al.* 2014a,b). *P*-wave amplitudes were corrected for sensor coupling quality using ultrasonic transmission measurements (Kwiatek *et al.* 2014b). Relative AE magnitudes were estimated as

$$M_{\mathrm{AE}} = \log_{10} \sqrt{\frac{1}{n} \sum_{i-1}^{n} (A_i R_i)^2}, \quad (1)$$

where A_i and R_i are wave amplitude and source-to-receiver distance to the sensor i, respectively (e.g. Zang *et al.* 1998). Following Dresen *et al.* (2020), we converted M_{AE} into the seismic moment and from that we calculated the moment magnitude M_{W}. In the following, the *P*-wave amplitudes were used to derive full moment tensors of selected events of highest quality (Kwiatek *et al.* 2014a, Goebel *et al.* 2015, 2017).

3.2 Data preparation

We analysed AE waveform data from 10 laboratory stick-slip failures that occurred during testing of samples W5 and S12. To estimate AE static stress drops ($\Delta\sigma_{\mathrm{AE}}$), we applied a variant of the spectral ratio technique (e.g. Ide *et al.* 2003; Abercrombie & Rice 2005) developed and tested for different seismic data sets including volcanic and induced seismicity (e.g. Kwiatek et al. 2011, 2014c, 2015; Harrington *et al.* 2015). The estimated corner frequencies (f_0) and seismic moments (M_{W}) were used to calculate relative static stress drops of AEs recorded in both experiments.

We selected a window of 256 (25.6 μs) samples from the AE waveforms starting shortly before the *P*-onset, removed the linear trend, and applied a two-sided von Hann's taper. Signal and noise windows were transferred to the Fourier domain using the multitaper method of Percival & Walden (1993). To meet the quality criteria, we selected spectra with a signal-to-noise ratio of at least 3 within a frequency band ($f_{\mathrm{min}}, f_{\mathrm{max}}$), with a maximum range between $f_{\mathrm{min}} \approx 7.8 \times 10^4$ and $f_{\mathrm{max}} \approx 5.0 \times 10^6$ Hz. For further analysis, we only considered AE events with at least six available spectra that met the criteria given above.

AE events with a sufficient number of spectra were further quality constrained. First, we selected events with a maximum location accuracy residuum ≤ 0.2 (± 2 mm hypocentre location accuracy) and for which a seismic moment tensor solution was available (e.g. Kwiatek *et al.* 2014a). Considering the location uncertainties, we restricted the catalogue to AE events occurring inside of the sample to exclude mislocated events. For sample W5, we also restricted AE locations close to the specimen main fault surface to better compare results with sample S12. Finally, we grouped AEs to large AE event populations according to stick-slip cycles and discarded AEs associated with large slip events (*cf.* Figs 1a and c).

3.3 Spectral ratio technique

For each grouped AE event population we computed spectral ratios based on linked AE event pairs (e.g. Kwiatek *et al.* 2011; Harrington *et al.* 2015). The event linkage was based on three criteria: (1) maximum allowed interevent distance d (i.e. colocated events), (2) minimum accepted magnitude difference ΔM between pairs of events and (3) minimum number of AE neighbours (number of links), $N_{\min}$. These quality parameters were coordinated carefully to maximize the empirical Green's function (eGf) criteria (e.g. Shearer *et al.* 2019). Due to the linking of several AE events, each AE could have numerous eGfs. Such multi-eGf links yielded more stable inversion results. The low AE activity per stick-slip in sample S12 restricted d to 15 mm. The high AE number in sample W5 allowed using $d \leq 3.7$ mm. The minimum magnitude difference for event pairs was $\Delta M \geq 0.3$ for S12 and $\Delta M \geq 0.4$ for W5. Finally, the AE events were linked by connecting each AE to at least five events within d and ΔM, which ensured inversion stability at moderate computational cost. The inversion problem relied on optimizing the cost function in the form (e.g. Kwiatek *et al.* 2015)

$$\text{Cost}\ (\Psi_{\text{th}}, \Psi_{\text{obs}}) = \sum_{i} \sum_{(j,k)} w_{ijk}\,(f)\ \ \| \Psi_{\text{th}}^{jk}\,(f) - \Psi_{\text{obs}}^{jk}\,(f) \|_{L1} = \ \min, \tag{2}$$

with

$$\Psi_{\text{th}}^{jk}\left(f;\ M_0^j,\ M_0^k,\ f_0^j,\ f_0^k\right) = \frac{S^j\left(f;\ M_0^j,\ f_0^j\right)}{S^k\left(f;\ M_0^k,\ f_0^k\right)} = \frac{M_0^j}{M_0^k}\left(\frac{1+\left(\frac{f}{f_0^j}\right)^4}{1+\left(\frac{f}{f_0^j}\right)^4}\right)^{\frac{1}{2}}, \tag{3}$$

to find relative seismic moment M_0 and corner frequency f_0 for each event in a population. We used the Boatwright (1978) source model in equation (3). Here, cubed measured velocities and spectral levels were used to estimate initial seismic moments. Differences between theoretical and observed spectral ratios, Ψ_{th} and Ψ_{obs}, of two linked AE event pairs *(j, k)* at sensor i, were weighted equally over all frequencies, using the coefficient w_{ijk}, as the original Fourier spectra $S(\cdot)$ in eq. (3) were interpolated to logarithmic domain beforehand. The weights were set to 0 whenever the signal-to-noise ratio from any observed spectra forming the pair (j, k) at station i was below 3 and therefore outside of the common frequency interval $(f_{\min 1}, f_{\max 1}) \cap (f_{\min 2}, f_{\max 2})$. The multidimensional inversion problem expressed by eq. (2) was solved using a simulated annealing approach based on non-stationary Metropolis–Hastings Random Walk (MHRW) algorithm (e.g. Sen & Stoffa 1995). The application of MHRW algorithm separately allowed calculating AE stress drop uncertainties. Representative samples of displacement spectra uncertainties are shown as heat maps for small, medium and large AE events in Fig. S1 (see Supporting Information).

To obtain results comparable to seismological studies at larger scales, we followed Kanamori (1977) to calculate the seismic moment magnitude:

$$M_W = \frac{\log_{10}(M_0) - 9.1}{1.5}\ . \tag{4}$$

AE stress drop estimates ($\Delta\sigma_{\text{AE}}$) were obtained following Eshelby (1957)

$$\Delta\sigma_{\text{AE}} = \frac{7}{16}\frac{M_0}{r^3}\ . \tag{5}$$

The source radius (rupture dimension) r was estimated from corner frequency measurements assuming the dynamic circular source model of Madariaga (1976):

$$r\ = \frac{C V_{ß}}{2\pi f_0}, \tag{6}$$

with $C = 1.32$. The S-wave velocity $V_{ß}$ was obtained from measured P-wave velocity V_{α} using:

$$V_{ß} = \frac{V_{\alpha}}{\sqrt{3}}\ . \tag{7}$$

4 RESULTS

4.1 Mechanical stress drop and AE activity relations

Each experiment resulted in six stick-slip events clearly indicated by large measured stress drops (LSDs) in the differential stress curve (Figs 1a and c). The LSDs observed in sample S12 first increase progressively with multiple slips but then remain constant. The post-slip minimum stress varies. Peak differential stresses of 400 MPa with maximum LSDs of approx. $\Delta\sigma_{\text{m}} \approx 300$ MPa are reached for stick-slips four and five. In contrast, maximum peak stress level for sample W5 stays roughly constant at about 290 MPa (∼25 per cent lower than in S12). Here, the LSDs increase progressively as the post-slip minimum decreases. A maximum stress drop of $\Delta\sigma_{\text{m}} \approx 190$ MPa (∼35 per cent less compared to S12) is reached for stick-slip number 5.

We observe differences in the AE event occurrence in relation with differential stress and time between both experiments. Sample W5 features a broader damage zone (*cf.* Goebel *et al.* 2014b) compared to specimen S12 (Figs 1b and d). Beyond yield stress, small mechanical stress drops (SSDs) are frequently observed prior to LSDs of the rough fault (Fig. 1c), clearly reflecting the larger fault complexity. Sample W5 shows continuously occurring AEs during the entire stick-slip cycle with an increased AE event rate related to large and small mechanical stress drops and reduced AE activity in the aftershock sequences (*cf.* Goebel *et al.* 2015). For this sample, we located a total number of 87 108 AEs. In contrast, sample S12 shows an increased AE activity only close to peak stress and LSDs without prominent aftershock sequences (*cf.* Kwiatek *et al.* 2014a). In total, 1268 AEs were located along the simple saw-cut fault plane (Fig. 1b). The stress–time curve (Fig. 1a) shows higher yield points, higher peak stress and no precursory SSDs as found in sample W5.

4.2 AE stress drops

We obtained source parameters (see also Blanke *et al.* 2020) of 688 AEs for sample S12 and 1882 AEs for sample W5 from the first five stick-slip cycles. The determined range of AE stress drops is between 0.01 and 100 MPa, which is comparable to the range in other studies (Fig. 2a). For sample S12, the estimated M_{W} and $\Delta\sigma_{\text{AE}}$ are slightly larger ($-9 < M_{\text{W}} < -5.6$ and $0.01 < \Delta\sigma_{\text{AE}} < 100$ MPa) than for W5 ($-9.1 < \text{M}_{\text{W}} < -6.6$ and $0.01 < \Delta\sigma_{\text{AE}} < 10$ MPa). However, in contrast to induced and natural seismicity shown in Fig. 2(a), we observe a systematic increase in $\Delta\sigma_{\text{AE}}$ with magnitude (Fig. 2a, inset). This dependence of $\Delta\sigma_{\text{AE}}$ on M_{W} is very pronounced in both lab data sets. Our data extend the magnitude ranges analysed in previous laboratory studies usually spanning only 1–2 orders of magnitude (see Fig. S2, Supporting Information). Noteworthy are the comparable stress drop estimates between this and previous studies for respective comparable magnitude ranges (Fig. S2, Supporting Information). We find that the observed M_{W}–$\Delta\sigma_{\text{AE}}$ relation is not affected by bandwidth limitation problems. The resolved corner frequencies are below 50 per cent of the maximum fitting frequency ($f_{\max} \approx 2 \times 10^6$ Hz), which is typically assumed to be 80 per cent of the Nyquist frequency ($f_{\text{Ny}} \approx 5 \times 10^6$ Hz) (e.g. Ruhl *et al.* 2017). In addition, even by excluding the smallest events, the

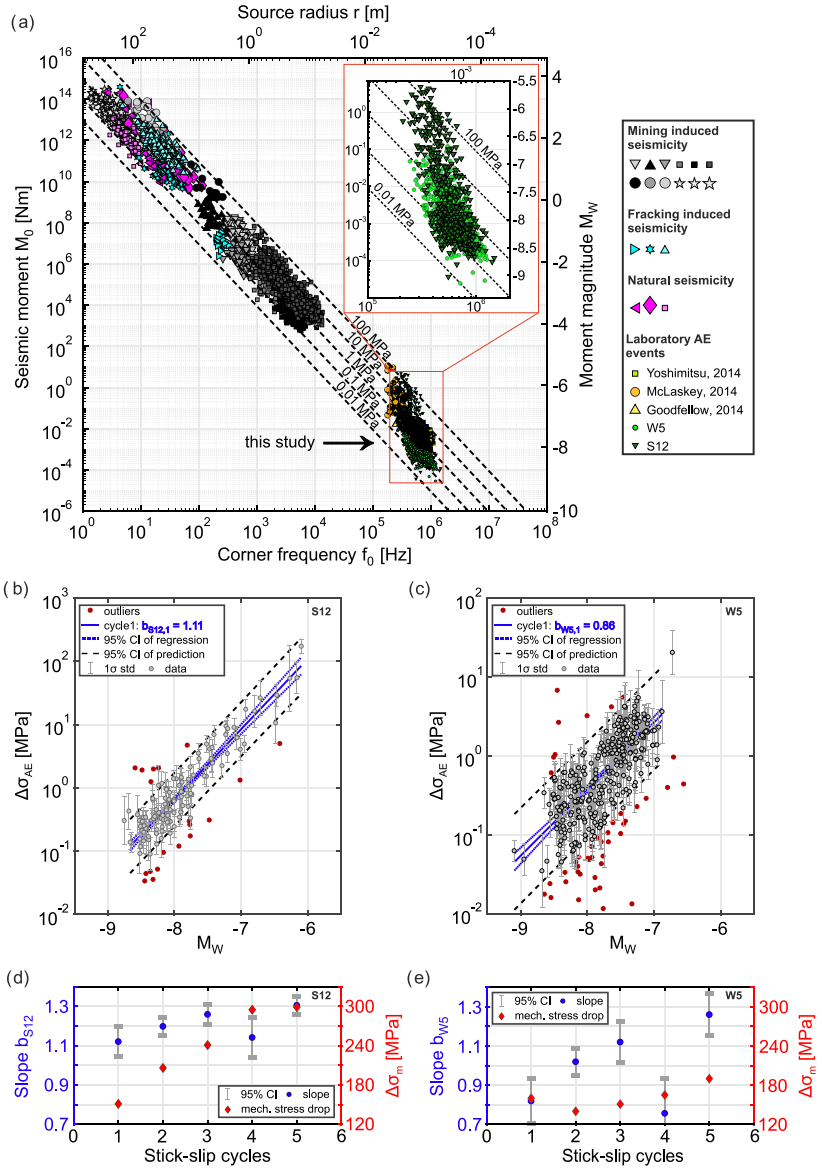

Figure 2. (a) Stress drop and source parameter relations, modified after Kwiatek *et al.* (2011), using the Madariaga (1976) source model. Colours separate 23 different studies of natural-, mining induced- and fracking induced seismicity, and laboratory AE events. This study results (green triangles and circles) are magnified in the inset. Dashed lines indicate constant stress drops of 0.01–100 MPa. (b) and (c) Regression analysis for interslip periods before the first stick-slip events (*cf.* highlighted rectangles in Figs 1a and c) of S12 and W5, respectively. Regression line (solid) is shown with 95 per cent CI of slope variance (dotted) and considered estimates used to calculate the slope (dashed). (d) and (e) M_W–$\Delta\sigma_{AE}$ slope changes per stick-slip cycle (circles). Diamonds represent mechanical stress drops for each stick-slip event (*cf.* Figs 1a and c).

observed dependency between M_W and $\Delta\sigma_{AE}$ remains (*cf.* Figs 2b and c).

We performed a least-squares linear regression analysis for both experiments on each individual interslip period (Figs 2b and c). Data points within a 95 per cent confidence interval (CI) were considered for the regression analysis and lower and upper bounds of the 95 per cent CI of the regression slope variation were calculated to visualize its possible variance. The sensitivity of $\Delta\sigma_{AE}$ to changes in M_w increases with consecutive stick-slip cycles, leading to an increase in slope (b) from 1.12 to 1.31 between the first and the last interslip period for S12 and an increase from $b = 0.82$ to 1.26 for sample W5 (Figs 2d and e). Consequently, while the average value of b is substantially larger for the smooth fault, the change in b with slip events is a factor of 2 larger for the rough fault. Sample S12 indicates a saturation of slope growth in the latest stick-slip cycles, analogous to the trend in mechanical stress drop $\Delta\sigma_m$ (Fig. 2d). Experiment W5 also shows similar behaviour between $\Delta\sigma_m$ and $\Delta\sigma_{AE}$ estimates but does not indicate saturation.

The overall size distribution of AEs can be linked to dominant length scales in the experiments. Minimum AE source radii, estimated from eq. (6), are approximately limited by the average grain sizes of Westerly granite (see Fig. 3). Differences in surface roughness expressed as rms of vertical topography (*cf.* Goebel *et al.* 2014a) in Fig. 3 seem to only play a secondary role in controlling minimum AE size.

The maximum size of events on the rough surface in sample W5 is similar to the width of the core deformation zone (maximum fault core width = 1.5–3 mm), providing here a plausible upper

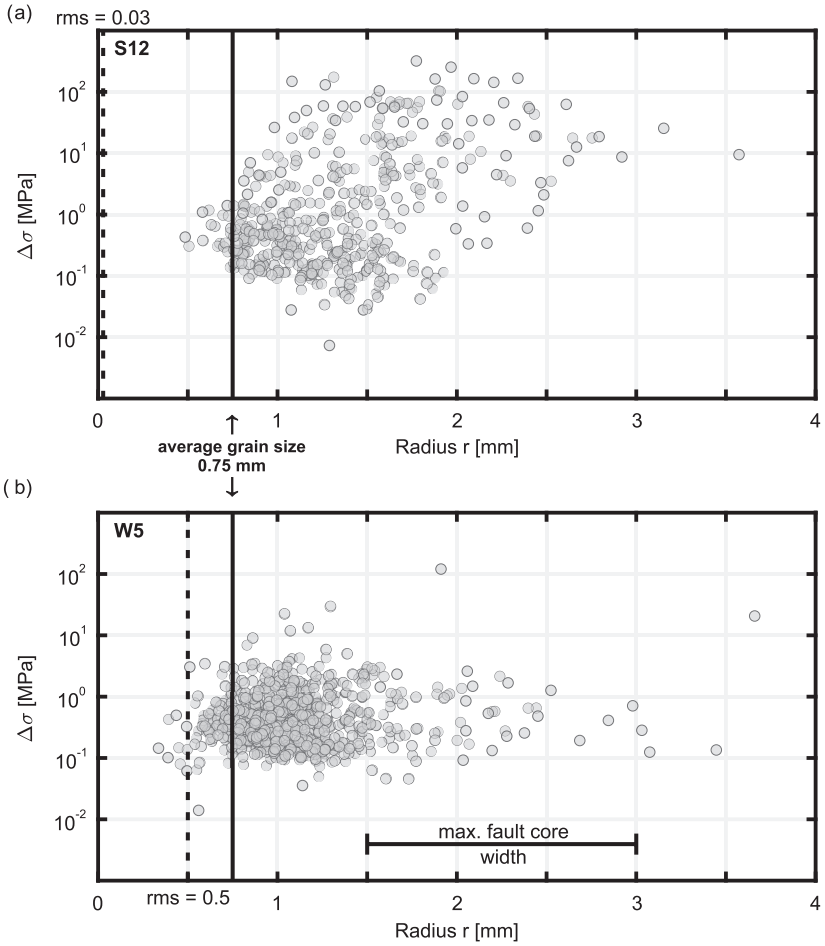

Figure 3. Source radii and static stress drop relation of (a) S12 and (b) W5. Red solid line indicates average grain size of Westerly granite. Dashed line shows rms of roughness from 2-D white-light interferometry measurement and black horizontal bar indicates maximum width of the fault core along the slip direction for sample W5.

bound for AE event growth. However, AEs on the smooth fault in sample S12 also grow to similar sizes, which are clearly beyond peak roughness wavelength and fault core width on S12. Such large events on S12 also result in substantially higher $\Delta\sigma_{AE}$ and show a dominance of earthquake-like double couple source mechanisms (Fig. S3, Supporting Information). Thus, while minimum event sizes in both experiments can potentially be linked to grain size distribution, the maximum seismic event size appears more sensitive to fault roughness with smoother faults producing large magnitude events with higher $\Delta\sigma_{AE}$.

5 DISCUSSION

Whether seismic stress drop of natural and induced seismicity varies with earthquake magnitude or remains constant is still a matter of debate. Although, stress drop estimates fall within a similar range of 0.01–100 MPa for events between M_W −9 and M_W 4 (Fig. 2), individual well-resolved data sets show variability potentially due to differences in underlying source processes. The present laboratory study clearly highlights a M_W–$\Delta\sigma_{AE}$ dependence (Figs 2d and e) beyond the commonly observed range of static stress drop variation (e.g. Abercrombie 2015) in individual data sets. This is in contrast to a majority of field studies that found a constant static stress drop independent of event magnitude (e.g. Ide & Beroza 2001; Prieto *et al.* 2004). In the following, we discuss potential effects, non-physical and physical, that may control the presented M_W–$\Delta\sigma_{AE}$ relation.

5.1 Non-physical effects

Non-physical parameters, related to data quality and analysis, may cause apparent dependence of stress drop on magnitude and errors in source parameter calculations (e.g. Ide & Beroza 2001; Abercrombie 2013). The list of potential factors includes large azimuthal gaps, inaccurate estimates of attenuation (Q), propagation effects, a limited magnitude range, bandwidth limitations or an inaccurate source model.

To minimize the error-term, we followed several instrumentational and analytical steps: (1) the laboratory setup allows us to design a seismic network that prevents large azimuthal gaps. This is accomplished by placing sensors all around the sample and the expected source region and not just along the surface, which is a common limitation for natural events. (2) We use the spectral ratio method that, if applied carefully, eliminates path and site effects. In addition, we explore the effect of using several eGfs for each event, which adds to the robustness of source spectra inversions. (3) Furthermore, our data cover a reasonably large magnitude range ($-9.1 < M_W < -5.6$), substantially expanding the magnitude span

of comparable previous AE studies (e.g. McLaskey *et al.* 2014; Yoshimitsu *et al.* 2014). (4) Lower and upper frequency bounds f_{min} and f_{max} define the range of resolvable frequencies of the AE spectra. Considering the careful selection of analysed AE events including a good signal-to-noise level, a large number of available recorded waveforms and estimated spectra, and the application of multi-eGf links for each analysed event, we consider a potential bandwidth problem unlikely. Even by excluding the smallest recorded events with magnitudes $M_W < -8.4$, the clear stress drop–magnitude dependence remains. (5) We use the commonly accepted circular shear source model of Boatwright (1978) to make our study comparable to previous work. However, we obtain stress drop estimates clearly exceeding the general observed variability.

5.2 Physical effects

Stress drop may be affected by changes in seismic source processes. Suggested factors influencing these processes address a strongly heterogeneous stress field (e.g. Candela *et al.* 2011; Wang *et al.* 2019), for example, induced by a complex fault geometry (roughness), and changes in rupture velocity (e.g. Kanamori & Rivera 2004). Rupture and also slip velocity may be affected by structural and material heterogeneities in the fault zone. However, potential effects from these factors have not yet been sufficiently investigated.

5.2.1 *Impact of fault surface roughness*

The main macroscopic difference between the experiments analysed in this study is the degree of fault roughness, which in turn leads to notable differences in AE rates, peak stresses, yield point and the extent of the work-hardening (inelastic) phase (Figs 1a and c). The smooth fault S12 (Fig. 1b), characterized by a simple homogeneous fault zone, indicates strong coupling of the saw-cut blocks. The fault remained fully locked up to almost peak stress, which is reflected by the extended linear mechanical stress increase (Figs 1a and b). During the elastic loading phase, AE activity remained very low with precursory activity only occurring after differential stresses exceeded the yield point (Fig. 1a). The resulting high peak stresses were released in slip events with LSDs.

In contrast, the rough fault W5 (Fig. 1d) exhibits a broader damage zone and an anastomosing network of slip surfaces (Goebel *et al.* 2012). The higher roughness likely results in relatively poor coupling of the fault blocks. The yield point occurred at lower stresses within the interslip periods and AE activity was high during loading and SSDs (Fig. 1c). Peak stresses at LSDs were 25 per cent lower than on the smooth surface. Similarly, $\Delta\sigma_m$ was about 35 per cent smaller.

The differences due to fault roughness are also reflected in AE source parameters. On the rough surface the maximum AE moment magnitudes ($M_{Wmax} \sim -6.6$) and stress drops ($\Delta\sigma_{AEmax} \sim 10$ MPa) are about one order smaller than on the smooth surface ($M_{Wmax} \sim -5.6$, $\Delta\sigma_{AEmax} \sim 100$ MPa). The smooth fault S12 shows a weak slope increase of M_W–$\Delta\sigma_{AE}$ regression lines as peak stress and $\Delta\sigma_m$ increase for the first four slip events (Fig. 2d). This may be related to conditioning of the saw-cut in combination with increasing formation of fault gouge. That likely causes the larger AE stress drops and greater moment magnitudes. The increase of $\Delta\sigma_m$ and M_W–$\Delta\sigma_{AE}$ regression slopes may saturate once a thin but stable gouge layer covers the slip surface. The rough fault W5 shows an increase of $\Delta\sigma_m$ and M_W–$\Delta\sigma_{AE}$ regression slopes possibly in response to a continuous destruction and smoothing of asperities. With large stick-slip events, asperities may be reduced as the slip planes become progressively smoother.

Interestingly, in both experiments the source radii of AEs are roughly bounded by the average grain size (Fig. 3). This suggests that $\Delta\sigma_{AE}$ is slip-controlled and may not scale with grain size or source radius. We discuss this hypothesis in more detail in the following section.

5.2.2 *Structural heterogeneity and grain size effects*

Grain scale structural heterogeneities may affect AE source radii that in turn affect static stress drops as expressed in eqs (5) and (6). In general, initial crack size in undeformed rock samples scales with grain size (e.g. Dresen & Evans 1993). The source radii of AEs observed in both samples range between 0.4 and 3.5 mm, which is on the order of grain size variation (Fig. 3). We do not observe a significant dependence of stress drop on source radius, with the exception of a weak trend for specimen S12. In contrast, the change in $\Delta\sigma_{AE}$ is large compared to the change in source radius. Therefore, we posit that observed $\Delta\sigma_{AE}$ variations may be mainly attributed to increasing slip over fracture surfaces correlated to grain size along grain boundaries for small events or across multiple grains for larger events (e.g. Candela *et al.* 2011). This is supported by the observed increase in complexity of source processes for smaller AE events (*cf.* Kwiatek *et al.* 2014a) displaying a significant contribution of non-double couple components of AE moment tensors (Fig. S3, Supporting Information). This again suggests that an increase of the mechanical stress drop, related to progressively increasing slip over the fault surface, translates to microscale fracture propagation and AE source characteristics (*cf.* Figs 2d and e, and 3).

5.2.3 *Rupture velocity*

Coalescence of cracks during rupture propagation may also result in higher rupture velocities as ruptures accelerate. For example, double-couple (simple shear motion) events occurring in sample S12 show high stress drops (Fig. S3, Supporting Information). In contrast, smaller events caused by crack propagation along grain boundaries and kinks may display only limited slip and are characterized by larger non-double-couple components. It is conceivable that during complex crack growth more energy is spent in crack surface energy and heat at the expense of radiated energy (Kanamori & Brodsky 2004). This could cause spatially variable seismic slips (e.g. Mai & Beroza 2002) independent of source radius but dependent on roughness (*cf.* Candela *et al.* 2011).

To test whether changes in rupture velocity (V_r) significantly affect our stress drop observations, we reduced V_r with decreasing M_W, using correction factors provided by Sato & Hirasawa (1973). We first adjusted source radii and stress drops using eqs (6) and (5), respectively. We then calculated a mean M_W–$\Delta\sigma_{AE}$ regression slope for each experiment by gathering AEs from all analysed AE populations. We reduced V_r to 50 per cent for the smallest AEs. By reducing AE rupture velocities from 90 per cent to 50 per cent, V_r shows only a small effect on M_W–$\Delta\sigma_{AE}$ regression slopes for sample S12 (Fig. S4, Supporting Information). The effect is slightly more visible for sample W5, due to an increase of stress drop for small events (*cf.* Kanamori & Rivera 2004). The still existing scaling clearly shows only a limited effect of V_r changes on the M_W–$\Delta\sigma_{AE}$ scaling relation. This suggests that the observed changes in stress drop may be related to complex rupture along a rough slip plane,

possibly leading to varying radiated energy and energy partitioning during slip.

5.3 Implications for tectonic earthquakes along fault zones

Few field studies have investigated the effect of fault maturity and related roughness evolution on earthquake source parameters (e.g. Ben-Zion & Sammis 2003; Şengör *et al.* 2005; Sagy *et al.* 2007; Brodsky *et al.* 2011; Bohnhoff *et al.* 2016). Geometric complexity is thought to decrease with increasing fault length of fault segments, finite displacement and age. Martínez-Garzón *et al.* (2015) showed that for strike-slip faults maximum observed earthquake magnitudes generally scale with total slip and fault length. Dynamic rupture models indicate that geometric complexity and associated stress field heterogeneity affect the entire source process from nucleation to rupture arrest and therefore also affect stress drop, rupture velocity and radiated energy (e.g. Ripperger *et al.* 2007).

Comparing our tests to field observations, a fresh fractured surface in the laboratory may be a good proxy for an 'immature' and complex natural fault zone (e.g. Kwiatek *et al.* 2014a; Goebel *et al.* 2017). A smooth saw-cut fault may serve as a laboratory analogue of a 'mature' fault that experienced extensive surface smoothing due to multiple seismic events over a long time-span. Nevertheless, upscaling laboratory observations to natural earthquakes remains challenging, not least due to the fact that characteristic length scales are very different between field and laboratory tests. Upscaling not only involves formulating appropriate constitutive laws for key physical processes observed in experiments but also some renormalization procedure allowing to formulate, for example, an effective friction law (Campillo *et al.* 2001). Furthermore, the actual roughness of natural faults at seismogenic depth is yet to be determined, which is an extremely challenging task. Thus, laboratory experiments that focus on key parameters related to seismic slip and stress drop variations will remain the only analogue of hazardous earthquakes along tectonic faults.

6 CONCLUSION

We investigated seismic and mechanical stress drop variations during triaxial stick-slip experiments on two faulted Westerly granite samples with different roughness. We cover a broad magnitude range of $-9 < M_W < -5.6$, which is substantially larger than in previous related AE studies. Using the spectral ratio method, we calculated AE stress drops which are within a comparable range of observations from induced and natural earthquakes up to $M_W = 4$. A key observation is the strong increase of AE static stress drop with AE magnitude, which differs from most source studies analysing natural seismicity and seems to be much more pronounced for AE events. This increase is most pronounced for AEs on smooth surfaces. The slope of the corresponding relationship between $\Delta\sigma_{AE}$ and M_W increases with consecutive stick-slips on rough surfaces. Mechanical stress drops also increase with successive slip events on rough and smooth surfaces potentially due to progressive surface smoothing. Average grain size and the width of the fault core provide approximate lower and upper bounds of AE sizes on rough surfaces. Large AE events on smooth fault surfaces exhibit the highest stress drops and are dominated by double-couple moment tensors. Our results indicate a direct coupling between the scale of heterogeneity (grain size, roughness and damage zone width) and seismic event characteristics in the laboratory. The experiments suggest that larger stress drops require mature, smooth faults, whereas rougher faults promote lower stress drop events. Similarly, crustal heterogeneity may be an important factor that governs earthquake stress drop variations in nature. This needs to be further investigated, in particular for hazard-prone plate-bounding earthquakes, given the large implications for the resulting risk to near-fault population centres and infrastructure.

ACKNOWLEDGEMENTS

We would like to thank the Editor Andrea Morelli and the Reviewers Art McGarr and Yihe Huang for helpful comments and suggestions. The experiments were conducted at GFZ German Research Centre for Geosciences. Data can be accessed via the GFZ Data Services (see Blanke *et al.* 2020) and by contacting the first author. This study has been partially funded by the H2020 project SERA (Seismology and Earthquake Engineering Research Infrastructure Alliance for Europe, grant agreement no. 730900). GK acknowledges support from the Deutsche Forschungsgemeinschaft (DFG), grant KW 84/4-1. The processing of data and generation of figures were done using MATLAB R2017a (https://www.mathworks.com/products/matlab.html, last accessed December 2019) and POV-RAY v3.7 (http://www.povray.org/, last accessed December 2019).

REFERENCES

Abercrombie, R.E., 1995. Earthquake source scaling relationship from -1 to 5 M_L using seismograms recorded at 2.5 km depth, *J. geophys. Res*., **100,** 24 015–24 036.

Abercrombie, R.E. & Rice, J.R., 2005. Can observations of earthquake scaling constrain slip weakening?, *Geophys. J. Int.,* **162,** 406–424.

Abercrombie, R.E., 2013. Comparison of direct and coda wave stress drop measurements for the Wells, Nevada, earthquake sequence, *J. geophys. Res. Solid Earth,* **118,** 1458–1470.

Abercrombie, R.E., 2015. Investigating uncertainties in empirical Green's function analysis of earthquake source parameters, *J. geophys. Res. Solid Earth,* **120,** 4263–4277.

Aki, K., 1967. Scaling law of seismic spectra, *J. geophys. Res.,* **72**(4), 1217–1231.

Allmann, B.P. & Shearer, P.M., 2009. Global variations of stress drop for moderate to large earthquakes, *J. geophys. Res.,* **114,** B01310, doi:10.1029/2008JB005821.

Baltay, A., Ide, S., Prieto, G. & Beroza, G., 2011. Variability in earthquake stress drop and apparent stress, *Geophys. Res. Lett.,* **38,** L06303, doi:10.1029/2011GL046698.

Baltay, A.S., Hanks, T.C. & Abrahamson, N.A., 2019. Earthquake stress drop and arias intensity, *J. geophys. Res.,* **124**(4), 3838–3852.

Beeler, N., 2006. Inferring earthquake source properties from laboratory observations and the scope of lab contributions to source physics, in *Earthquakes: Radiated Energy and the Physics of Faulting,* pp. 99–119, eds. Abercrombie, R., McGarr, A., Di Toro, G. & Kanamori, H., AGU, Washington, DC.

Ben-Zion, Y. & Sammis, C.G., 2003. Characterization of fault zones, *Pure appl. Geophys.,* **160,** 677–715.

Blanke, A., Goebel, T. & Kwiatek, G., 2020. Acoustic emission source parameters of laboratory triaxial stick-slip experiments on two Westerly granite samples, GFZ Data Services, https://doi.org/10.5880/GFZ.4.2.2020.008.

Boatwright, J., 1978. Detailed spectral analysis of two small New York State earthquakes, *Bull. seism. Soc. Am.,* **68,** 1131–1177.

Bohnhoff, M., Dresen, G., Ellsworth, W.L. & Ito, H., 2009. Passive seismic monitoring of natural and induced earthquakes: case studies, future directions and socio-economic relevance, in *New Frontiers in Integrated Solid Earth Sci.,* pp. 261–285, eds. Cloetingh, S. & Negendank, J., Springer, Dordrecht.

Bohnhoff, M., Martínez-Garzón, P., Bulut, F., Stierle, E. & Ben-Zion, Y., 2016. Maximum earthquake magnitudes along different sections of the North Anatolian fault zone, *Tectonophysics,* **674,** 147–165.

Brace, W.F. & Byerlee, J.D., 1966. Stick-slip as a mechanism for earthquakes, *Science,* **153**(3739), 990–992.

Brodsky, E.E., Gilchrist, J.J., Sagy, A. & Collettini, C., 2011. Faults smooth gradually as a function of slip, *Earth planet. Sci. Lett,* **302,** 185–193.

Brune, J.N., 1970. Tectonic stress and the spectra of seismic shear waves from earthquakes, *J. geophys. Res.,* **75**(26), 4997–5009.

Campillo, M., Favreau, P., Ionescu, I.R. & Voisin, C., 2001. On the effective friction law of a heterogeneous fault, *J. geophys. Res.,* **106**(B8), 16 307–16 322.

Candela, T., Renard, F., Bouchon, M., Schmittbuhl, J. & Brodsky, E.E., 2011. Stress drop during earthquakes: Effect of fault roughness scaling, *Bull. seism. Soc. Am.,* **101**(5), 2369–2387.

Cocco, M., Tinti, E. & Antonella, C., 2016. On the scale dependence of earthquake stress drop, *J. Seismol.,* **20**(4), 1151–1170.

Cotton, F., Archuleta, R. & Causse, M., 2013. What is sigma of the stress drop?, *Seismol. Res. Lett.,* **84**(1), 42–48.

Dresen, G. & Evans, B., 1993. Brittle and semibrittle deformation of synthetic marbles composed of two phases, *J. geophys. Res.,* **98**(B7), 11 921–11 933.

Dresen, G., Kwiatek, G., Goebel, T.H.W. & Ben-Zion, Y., 2020. Partitioning of seismic and aseismic preparatory processes before stick-slip failure, *Pure appl. Geophys.,* https://doi.org/10.1007/s00024-020-02605-x.

Eshelby, J.D., 1957. The determination of the elastic field of an ellipsoidal inclusion, and related problems, *Proc. R. Soc. Lond. A.,* **241,** 376–396.

Goebel, T.H.W., Becker, T.W., Schorlemmer, D., Stanchits, S., Sammis, C., Rybacki, E. & Dresen, G., 2012. Identifying fault heterogeneity through mapping spatial anomalies in acoustic emission statistics, *J. geophys. Res.,* **117,** B03310, doi:10.1029/2011JB008763.

Goebel, T.H.W., Schorlemmer, D., Becker, T.W., Dresen, G. & Sammis, C.G., 2013. Acoustic emission document stress changes over many seismic cycles in stick-slip experiments, *Geophys. Res. Lett.,* **40,** 2049–2054.

Goebel, T.H.W., Candela, T., Sammis, C.G., Becker, T.W., Dresen, G. & Schorlemmer, D., 2014a. Seismic event distributions and off-fault damage during frictional sliding of saw-cut surfaces with pre-defined roughness, *Geophys. J. Int.,* **196,** 612–625.

Goebel, T.H.W., Becker, T.W., Sammis, C.G., Dresen, G. & Schorlemmer, D., 2014b. Off-fault damage and acoustic emission distribution during the evolution of structurally complex faults over series of stick-slip events, *Geophys. J. Int.,* **197,** 1705–1718.

Goebel, T.H.W., Sammis, C.G., Becker, T.W., Dresen, G. & Schorlemmer, D., 2015. A comparison of seismicity characteristics and fault structure between stick-slip experiments and nature, *Pure appl. Geophys.,* **172,** 2247–2264.

Goebel, T.H.W., Kwiatek, G., Becker, T.W., Brodsky, E.E. & Dresen, G., 2017. What allows seismic events to grow big?: insights from b-value and fault roughness analysis in laboratory stick-slip experiments, *Geology,* **45**(9), 815–818.

Goodfellow, S.D. & Young, R.P., 2014. A laboratory acoustic emission experiment under in situ conditions, *Geophys. Res. Lett.,* **41,** 3422–3430.

Harrington, R.M., Kwiatek, G. & Moran, S.C., 2015. Self-similar rupture implied by scaling properties of volcanic earthquakes occurring during the 2004–2008 eruption of Mount St. Helens, Washington, *J. geophys. Res. Solid Earth,* **120,** doi:10.1002/2014JB011744.

Huang, Y., Beroza, G.C. & Ellsworth, W.L., 2016. Stress drop estimates of potentially induced earthquakes in the Guy-Greenbrier sequence, *J. geophys. Res. Solid Earth,* **121,** 65597–66607.

Huang, Y., Ellsworth, W.L. & Beroza, G.C., 2017. Stress drops of induced and tectonic earthquakes in the central United States are indistinguishable, *Sci. Adv.,* **3**(8), doi:10.1126/sciadv.1700772.

Ide, S. & Beroza, G.C., 2001. Does apparent stress vary with earthquake size?, *Geophys. Res. Lett.,* **28**(17), 3349–3352.

Ide, S., Beroza, G.C., Prejean, S.G. & Ellsworth, W.L., 2003. Apparent break in earthquake scaling due to path and site effects on deep borehole recordings, *J. geophys. Res.,* **108**(B5), 2271, doi:10.1029/2001JB001617.

Kanamori, H., 1977. The energy released in great earthquakes, *J. geophys. Res.,* **82**(20), 2981–2987.

Kanamori, H. & Brodsky, E.E., 2004. The physics of earthquakes, *Rep. Prog. Phys.,* **67,** 1429–1496.

Kanamori, H. & Rivera, L., 2004. Static and dynamic scaling relations for earthquakes and their implications for rupture speed and stress drop, *Bull. seism. Soc. Am.,* **94**(1), 314–319.

Kanamori, H. & Rivera, L., 2006. Energy partitioning during an earthquake, In Earthquakes: Radiated Energy and the Physics of Faulting (eds R. Abercrombie, A. McGarr, G. Di Toro & H. Kanamori), *Geophys. Monogr. Ser.,* Vol. **170,** pp. 3–13, Washington, DC: AGU.

Kwiatek, G., Plenkers, K., Dresen, G. &JAGUARS Research Group, 2011. Source parameters of picoseismicity recorded at Mponeng Deep Gold Mine, South Africa: implications for scaling relations, *Bull. seism. Soc. Am.,* **101**(6), 2592–2608.

Kwiatek, G., Goebel, T.H.W. & Dresen, G., 2014a. Seismic moment tensor and b value variations over successive seismic cycles in laboratory stick-slip experiments, *Geophys. Res. Lett.,* **41,** 5838–5846.

Kwiatek, G., Charalampidou, E.-M., Dresen, G. & Stanchits, S., 2014b. An improved method for seismic moment tensor inversion of acoustic emissions through assessment of sensor coupling and sensitivity to incidence angle, *Int. J. Rock Mech. Min. Sci.,* **65,** 153–161.

Kwiatek, G., Bulut, F., Bohnhoff, M. & Dresen, G., 2014c. High-resolution analysis of seismicity induced at Berlín geothermal field, El Salvador, *Geothermics,* **52,** 98–111.

Kwiatek, G., Martínez-Garzón, P., Dresen, G., Bohnhoff, M., Sone, H. & Hartline, C., 2015. Effects of long-term fluid injection on induced seismicity parameters and maximum magnitude in northwestern part of The Geysers geothermal field, *J. geophys. Res. Solid Earth,* **120,** 7085–7101.

Madariaga, R., 1976. Dynamics of an expanding circular fault, *Bull. seism. Soc. Am.,* **66**(3), 639–666.

Mai, P.M. & Beroza, G.C., 2002. A spatial random field model to characterize complexity in earthquake slip, *J. geophys. Res.,* **107**(B11), ESE 10–11-ESE 10-21.

Martínez-Garzón, P., Bohnhoff, M., Ben-Zion, Y. & Dresen, G., 2015. Scaling of maximum observed magnitudes with geometrical and stress properties of strike-slip faults, *Geophys. Res. Lett.,* **42,** 10,230–210,238.

McGarr, A. & Fletcher, J.B., 2003. Maximum slip in earthquake fault zones, apparent stress, and stick-slip friction, *Bull. seism. Soc. Am.,* **93**(6), 2355–2362.

McLaskey, G.C., Kilgore, B.D., Lockner, D.A. & Beeler, N.M., 2014. Laboratory generated M -6 earthquakes, *Pure appl. Geophys.,* **171,** 2601–2615.

Percival, D.B. & Walden, A.T., 1993. *Spectral Analysis for Physical Applications: Multitaper and Conventional Univariate Techniques,* Cambridge University Press, doi:10.1017/CB09780511622762.

Plenkers, K., Schorlemmer, D. & Kwiatek, G. the JAGUARS Research Group, 2011. On the probability of detecting picoseismicity, *Bull. seism. Soc. Am.,* **101**(6), 2579–2591.

Prieto, G., Shearer, P.M., Vernon, F.L. & Kilb, D., 2004. Earthquake source scaling and self-similarity estimation from stacking P and S spectra, *J. geophys. Res.,* **109,** B08310, doi: 10.1029/2004JB003084.

Ripperger, J., Ampuero, J.-P., Mai, P.M. & Giardini, D., 2007. Earthquake source characteristics from dynamic rupture with constrained stochastic fault stress, *J. geophys. Res.,* **112,** B04311, doi:10.1029/2006JB004515.

Ruhl, C.J., Abercrombie, R.E. & Smith, K.D., 2017. Spatiotemporal variation of stress drop during the 2008 Mogul, Nevada, earthquake swarm, *J. geophys. Res. Solid Earth,* **122,** 8163–8180.

Sagy, A., Brodsky, E.E. & Axen, G.J., 2007. Evolution of fault-surface roughness with slip, *Geology,* **35**(3), 283–286.

Sato, T. & Hirasawa, T., 1973. Body wave spectra from propagating shear cracks, *J. Phys. Earth,* **21,** 415–431.

Sen, P. & Stoffa, L., 1995. *Global Optimization Methods in Geophysical Inversion, Advances in Exploration Geophysics,* vol. **4,** 1st edition, Elsevier Science, Amsterdam.

Şengör, A.M.C., Tuysuz, O., Imren, C., Sakinc, M., Eyidogan, H., Gorur, G., Le Pichon, X. & Rangin, C., 2005. The North Anatolian fault: a new look, *Annu. Rev. Earth planet. Sci.,* **33,** 37–112.

Shearer, P.M., Abercrombie, R.E., Trugman, D.T. & Wang, W., 2019. Comparing EGF methods for estimating corner frequency and stress drop from P wave spectra, *J. geophys. Res. Solid Earth,* **124,** 3966–3986.

Spottiswoode, S.M., 1993. Seismic attenuation in deep-level mines, in: *Proceedings of the 3rd International Symposium on Rockbursts and Seismicity in Mines,* pp. 409–414, ed. Young, R.P., Kingston, Canada, Balkema, Rotterdam.

Stanchits, S., Vinciguerra, S. & Dresen, G., 2006. Ultrasonic velocities, acoustic emission characteristics and crack damage of basalt and granite, *Pure appl. Geophys.,* **163**(5-6), 975–994.

Thompson, B.D., Young, R.P. & Lockner, D.A., 2009. Premonitory acoustic emissions and stick-slip in natural and smooth-faulted Westerly granite, *J. geophys. Res.,* **114,** B02205, doi:10.1029/2008JB005753.

Tullis, J. & Yund, R.A., 1977. Experimental deformation of dry Westerly granite, *J. geophys. Res.,* **82**(36), 5705–5718.

Wang, H., Ren, Y., Wen, R. & Xu, P., 2019. Breakdown of earthquake self-similar scaling and source rupture directivity in the 2016–2017 central Italy seismic sequence, *J. geophys. Res. Solid Earth,* **124,** 3898–3917.

Yoshimitsu, N., Kawakata, H. & Takahashi, N., 2014. Magnitude –7 level earthquakes: a new lower limit of self-similarity in seismic scaling relationships, *Geophys. Res. Lett.,* **41,** 4495–4502.

Zang, A.F., Wagner, F.C., Stanchits, S., Dresen, G., Andersen, R. & Haidekker, M.A., 1998. Source analysis of acoustic emissions in Aue granite cores under symmetric and asymmetric compressive loads, *Geophys. J. Int.,* **135**(3), 1113–1130.

SUPPORTING INFORMATION

Supplementary data are available at *GJI* online.

Figure S1: AE waveforms of (a) a large ($M_W = -5.7$), (b) a medium ($M_W = -7.5$) and (c) a small ($M_W = -8.7$) AE event. Highlighted are the *P*-onset pick (red), the selected waveform window (blue) and the reference noise signal (grey) used for the inversion. Subfigures (d)–(f) visualize the corresponding average observed spectra (blue line) with average noise level (grey line) and the source parameter fitting. Grey dots show the MHRW-sampled corner frequency–seismic moment pairs representing uncertainties of estimated source parameters. Pink solid vertical and horizontal lines indicate maximum likelihood solution. Black thick solid line shows the corresponding optimum spectral fit. Dark and light shaded parts indicate heat map of spectral fits showing optimal and non-optimal fitting areas, respectively. Black dashed lines constrain the area of acceptable spectral fittings (95 per cent CI).

Figure S2: Magnification of laboratory AE study results from Fig. 2(a). Seismic source parameter relations from (a) this study with circles indicating results of W5 and triangles showing results of S12, (b) Yoshimitsu *et al.* (2014), (c) McLaskey *et al.* (2014) and (d) Goodfellow & Young (2014). Dashed lines indicate constant stress drops ($\Delta\sigma_{AE}$) of 0.01–100 MPa. Note this study (Fig. S2a) shows a broader span of magnitudes and corner frequencies and a larger number of AE events. A static stress drop dependence on event size is visible. This study covers the magnitude ranges of the other shown laboratory studies. Comparable static stress drop estimates for same magnitude ranges are obtained.

Figure S3: Relation of estimated AE moment magnitudes and ISO component percentages of full moment tensor solutions of experiment S12 (modified after Kwiatek *et al.* 2014a). Data shown here, are gathered from all stick-slip cycles and colour-coded by their stress drop estimates ($\Delta\sigma_{AE}$). Solid line indicates median ISO component estimated per 0.1 magnitude bin. Note the relationship between low stress drop estimates, small AE magnitudes and larger negative amount of ISO component and vice versa.

Figure S4: Regression slope changes caused by a rupture velocity reduction for small AEs. AE events of all AE populations were gathered to show the mean slope for (a) S12 and (b) W5. Solid lines are calculated using Sato & Hirasawa (1973) constants for 0.9 V_r rupture velocity. Dashed lines show the changed slope for 0.5 V_r. Arrows indicate a shift (increase) in static stress drop ($\Delta\sigma_{AE}$).

Please note: Oxford University Press is not responsible for the content or functionality of any supporting materials supplied by the authors. Any queries (other than missing material) should be directed to the corresponding author for the paper.